A Dual-Boundary-Tracking Finite Element Method for the Lamm Equation in Sedimentation Velocity Analytical Ultracentrifugation⋆

Chengshi Zeng[a], Xinqi Gong[b,*] and Wenqi Li[a,**]

[a]Beijing Frontier Research Center for Biological Structure, School of Life Sciences, Tsinghua University, Beijing, China
[b]School of Mathematics, Renmin University of China, Beijing, China

ARTICLE INFO

Keywords:
Analytical ultracentrifugation
Sedimentation velocity
Lamm equation
Finite element method
Nonuniform grid
Active-node selection

ABSTRACT

Analytical ultracentrifugation (AUC) is widely used to characterize the size distributions of proteins and other biological macromolecules. Quantitative analysis of sedimentation velocity data requires numerical solution of the finite-column Lamm equation, with adequate resolution of the migrating sedimentation boundary and, where relevant, the bottom back-diffusion region. Computational efficiency is therefore important, particularly because sedimentation-velocity analysis can require repeated solution of the Lamm equation during parameter estimation and distribution analysis. A dual-boundary-tracking finite element method (DBTFEM) is developed that combines a fixed, physically informed nonuniform radial grid with prediction-assisted dynamic selection of active nodes. The migrating sedimentation-boundary and bottom regions are retained as two coupled active blocks, while concentrations in the masked solution plateau are reconstructed analytically. This formulation concentrates the numerical solve on dynamically relevant regions of the radial domain while retaining the underlying finite element framework. The method is evaluated using six ideal, non-interacting sedimentation cases spanning different transport regimes and is compared with high-resolution numerical reference solutions. DBTFEM reproduces the interior concentration profiles accurately while substantially reducing the number of active spatial degrees of freedom in cases where the sedimentation and bottom regions remain sufficiently separated. Separate comparisons of grid allocation and active-node masking show that the benefit of the nonuniform grid is profile dependent, with the largest improvements obtained for steep sedimentation boundaries, whereas broader profiles exhibit accuracy comparable to that obtained with conventional uniform grids. Overall, DBTFEM provides an efficient finite element framework for finite-column Lamm equation simulation by combining physically informed spatial resolution with dynamic reduction of the active solution space.

1. Introduction

Analytical ultracentrifugation (AUC) is operated either in a sedimentation equilibrium configuration, in which net transport has ceased and the stable concentration gradient is analyzed [1], or in the sedimentation velocity configuration considered here. Sedimentation velocity analytical ultracentrifugation (SV-AUC) records the time evolution of radial concentration profiles in a sector-shaped solution column held in a strong centrifugal field. The sedimentation coefficient relates solute migration to the centrifugal field and depends on buoyant molar mass and hydrodynamic friction. Together with diffusional spreading, the measured profiles provide information about solute size, shape, and heterogeneity [2–4]. For a single ideal, non-interacting solute, transport is described by the Lamm equation [5], with sedimentation velocity $s\omega^2 r$ and diffusion coefficient D. The transient profile depends on these transport parameters, elapsed time, initial loading, and the column geometry and boundary conditions [3, 6].

*Corresponding author
**Principal corresponding author
zengchengshi@tsinghua.edu.cn (C. Zeng); xinqigong@ruc.edu.cn (X. Gong); liwenqi@tsinghua.edu.cn (W. Li)
ORCID(s): 0000-0003-4120-4440 (C. Zeng); 0000-0003-2802-6176 (X. Gong); 0009-0007-3140-6045 (W. Li)

Information can be extracted from sedimentation profiles through boundary-analysis procedures or direct numerical modeling. Examples of the former include van Holde–Weischet boundary extrapolation and the time-derivative analysis introduced by Stafford [7, 8]. Alternatively, numerical Lamm-equation solutions can be fitted directly to the experimental scans. Under the assumptions of the chosen model, this approach accounts for diffusional spreading when estimating sedimentation coefficient distributions [9] and can be extended to two-dimensional size-and-shape analyses [10, 11]. Direct modeling requires repeated forward solutions across candidate transport parameters or the basis functions used in distribution analysis [9, 11]. The numerical error of these solutions can affect the fitted profiles, while their computational cost constrains the number of evaluations that can be performed within a given budget. This motivates methods that characterize both solution error and computational effort [12–14].

The evolving concentration profile can contain regions with markedly different spatial scales. For initially uniform loading, sedimentation may produce a depleted region behind a migrating boundary, while solute accumulation near the cell bottom drives diffusion toward smaller radii [6, 13]. The extent and separation of these regions depend on the transport parameters and elapsed time, well-separated plateaus need not persist in diffusion-dominated cases. A uniform grid fine enough to resolve the steepest gradient

therefore allocates many of its degrees of freedom to the comparatively smooth plateau region.

Numerical schemes for the Lamm equation differ primarily in their treatment of the distinct spatial and temporal scales of sedimentation and diffusion. Finite-difference procedures on fixed radial grids were among the earliest approaches [15]. Claverie, Dreux, and Cohen then introduced the finite element discretization that has since become standard: a Galerkin formulation with continuous piecewise-linear (hat) basis functions on a fixed uniform mesh, yielding tridiagonal mass and transport matrices with entries computed from element integrals [16]. Because it was derived for systems of complete Lamm equations, the same formulation also accommodates interacting species. Fixed-grid solutions of this type were subsequently developed into practical tools for direct fitting [6, 17]. Moving-grid formulations relocate mesh nodes with the migrating sedimentation boundary, thereby concentrating spatial resolution near the evolving front, but require separate treatment of the fixed physical boundaries [6, 18]. Adaptive space-time finite element methods (ASTFEM) combine moving-grid transport resolution with treatment of the cell-bottom region [12, 19]. Brown and Schuck instead derived grid spacing from physical boundary-spreading scales and introduced active and inactive grid points [13]. Characteristic finite element formulations with local mesh refinement provide a further approach [14]. These studies establish the motivation for allocating resolution according to transport scales and for avoiding unnecessary calculations in smooth regions.

The choice of physical domain is coupled to these discretization schemes. A semi-infinite-column approximation is appropriate when the influence of the bottom boundary is negligible over the analyzed radial interval [13]. A finite-column model with zero-flux endpoints is required to describe bottom accumulation and its feedback on the interior profile [6, 12]. In that setting the bottom region must be retained numerically even when it spans only part of the column, so reducing the solved node set requires specifying how this region is coupled to the sedimentation boundary across the plateau. In addition to these spatial considerations, the temporal discretization also contributes to the overall numerical error. The present formulation employs Crank-Nicolson time integration [6, 20]. At fixed spatial resolution, temporal refinement eventually reaches an error floor determined by the spatial discretization and other approximation steps. Conversely, spatial refinement with a fixed time step may retain a non-negligible contribution from temporal discretization. These observations motivate separate temporal and spatial refinement studies and careful interpretation of the errors observed for the fully discrete scheme.

Beyond numerical discretization errors, the governing transport model itself relies on several simplifying physical assumptions. The present study is restricted to ideal, non-interacting solutes with constant sedimentation and diffusion coefficients under constant rotor speed. Concentration-dependent transport requires a generalized formulation, whereas reversible association may require coupled transport-reaction equations [16, 19, 21]. Experimental analysis must also account for systematic noise and instrumental effects, which may be addressed through preprocessing or incorporated directly into the fitting procedure [22, 23].

Within this setting, a dual-boundary-tracking finite element method (DBTFEM) is developed that combines a fixed nonuniform radial grid based on characteristic physical length scales with prediction-assisted active-node selection and analytical reconstruction of masked plateau concentrations. The two retained solution regions are coupled by a bridge element within a standard linear finite element formulation. In this way, the method integrates physically informed grid construction with dynamic active-region management without altering the underlying finite element framework.

The numerical evaluation is designed to separate the effects of grid allocation from those of active-node masking. Six benchmark cases are examined, together with a separate assessment of time-step sensitivity. Accuracy is quantified using both interior and complete-array profile deviations, while mass conservation, concentration positivity, and active-node statistics are evaluated at the prescribed output times.

2. Methods

2.1. Model problem and finite element discretization

We consider a single ideal, non-interacting solute in a sector-shaped solution column extending from the meniscus radius r_m to the cell bottom radius r_b. The sedimentation coefficient $s > 0$, diffusion coefficient $D > 0$, and rotor angular velocity ω are constant. The concentration $c(r,t)$ satisfies the Lamm equation [5]

$$\frac{\partial c}{\partial t} = \frac{1}{r}\frac{\partial}{\partial r}\left(rD\frac{\partial c}{\partial r} - s\omega^2 r^2 c\right), \qquad r_m < r < r_b, \quad (1)$$

with uniform initial concentration,

$$c(r,0) = c_0, \quad (2)$$

and zero solute flux at both physical boundaries,

$$j = s\omega^2 rc - D\frac{\partial c}{\partial r}, \qquad j(r_m,t) = j(r_b,t) = 0. \quad (3)$$

All reported calculations use unit loading, $c_0 = 1$, so that the computed concentration is numerically identical to the normalized concentration c/c_0. Rotor speeds specified in revolutions per minute (rpm) are converted to angular velocity according to $\omega = 2\pi n_{\mathrm{rpm}}/60$.

The spatial discretization follows the piecewise linear finite element formulation [6, 16]. On an ordered grid $r_m = r_1 < \cdots < r_N = r_b$, the concentration is approximated as

$$c_h(r,t) = \sum_{j=1}^{N} c_j(t)\phi_j(r), \quad (4)$$

where $\phi_j(r)$ denotes the continuous piecewise linear nodal basis function associated with node r_j, as illustrated in Fig. 1(a). And the complete set of basis functions defined on the underlying radial grid is shown in Fig. 1(b). Multiplying Eq. (1) by the weighted test function $r\phi_k$, integrating over the radial domain, and applying integration by parts together with the zero-flux boundary conditions yields

$$\int_{r_m}^{r_b} r\phi_k \frac{\partial c_h}{\partial t}\, dr = -D \int_{r_m}^{r_b} r\phi_k' \frac{\partial c_h}{\partial r}\, dr + s\omega^2 \int_{r_m}^{r_b} r^2 \phi_k' c_h\, dr. \tag{5}$$

The resulting semidiscrete system can be written as

$$\mathbf{B}\dot{\mathbf{c}} = \mathbf{J}\mathbf{c}, \qquad \mathbf{J} = s\omega^2 \mathbf{A}^{(2)} - D\mathbf{A}^{(1)}, \tag{6}$$

where

$$B_{kj} = \int_{r_m}^{r_b} \phi_j \phi_k r\, dr, \tag{7}$$

$$A^{(1)}_{kj} = \int_{r_m}^{r_b} \phi_j' \phi_k' r\, dr, \tag{8}$$

$$A^{(2)}_{kj} = \int_{r_m}^{r_b} \phi_j \phi_k' r^2\, dr. \tag{9}$$

All matrix entries are evaluated analytically from closed-form element integrals. Because the piecewise linear basis functions have local support, $\mathbf{B}$, $\mathbf{A}^{(1)}$, and $\mathbf{A}^{(2)}$ are tridiagonal and are stored using their three nonzero diagonals. Since the spatial grid remains fixed over a time step, this structure is reused at every step, and Crank-Nicolson integration reduces to

$$(2\mathbf{B} - \Delta t\, \mathbf{J})\mathbf{c}^{n+1} = (2\mathbf{B} + \Delta t\, \mathbf{J})\mathbf{c}^{n}. \tag{10}$$

The resulting tridiagonal linear system is solved using the Thomas algorithm. In the full-grid formulation, the system matrix is unchanged as long as the spatial grid, transport coefficients, rotor speed, and time step remain fixed, allowing its factorization to be reused across time steps. In the reduced-grid formulation, changes in the active-node set modify the discrete system, and the corresponding tridiagonal system is therefore assembled and solved for the active grid whenever the active-node set changes. Any valid numerical solution must preserve the physical conservation law for the sector-shaped column,

$$M(t) = \int_{r_m}^{r_b} c(r,t) r\, dr = \frac{c_0}{2}(r_b^2 - r_m^2). \tag{11}$$

Constant geometric factors are omitted. This continuum identity is distinguished from the conservation properties of the masking and reconstruction operations described below.

2.2. Physically informed nonuniform radial grid

The nonuniform radial grid is constructed according to the characteristic spatial variation of the concentration profile. Increased resolution is assigned near the meniscus and the cell bottom, where steep concentration gradients are most likely to develop. Between these regions, the local grid spacing is determined by the expected spreading of the sedimentation boundary arising from the combined effects of sedimentation and diffusion. The resulting grid concentrates spatial resolution where the solution is expected to vary most rapidly while avoiding unnecessary refinement in more slowly varying regions.

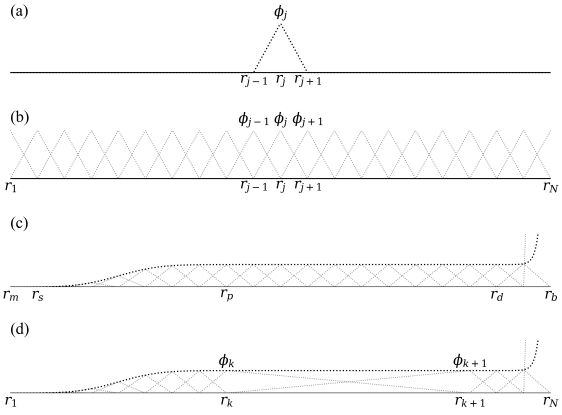

Figure 1: Finite element representation and active-grid reduction. (a) The continuous piecewise linear nodal basis function ϕ_j associated with radius node r_j, with support on $[r_{j-1}, r_{j+1}]$. (b) Basis functions on the underlying grid. (c) The sedimentation boundary region $[r_s, r_p]$ and bottom back-diffusion boundary region $[r_d, r_b]$, separated by a solution plateau. (d) A bridge element connects retained nodes across the masked solution plateau. During reconstruction, masked solution-plateau nodes are assigned the analytical dilution concentration. The schematic does not represent a conservative projection.

Physical scales and base spacing. To construct the nonuniform radial grid, characteristic length scales are derived from the sedimentation and diffusion parameters. Define

$$a = s\omega^2, \qquad \nu = a/D, \qquad A = (r_b^2 - r_m^2)/2. \tag{12}$$

For the finite column with zero-flux boundaries, the corresponding equilibrium concentration profile is

$$c_\infty(r) = c_0 \frac{\nu A}{1 - \exp(-\nu A)} \exp\left[-\frac{\nu}{2}(r_b^2 - r^2)\right]. \tag{13}$$

The radius at which the equilibrium concentration equals the initial loading, $c_\infty(r_e) = c_0$, is

$$r_e = \left[r_b^2 - \frac{2}{\nu} \ln\left(\frac{\nu A}{1 - \exp(-\nu A)}\right)\right]^{1/2}. \tag{14}$$

This radius provides a characteristic measure of the radial extent over which bottom accumulation and back-diffusion influence the equilibrium profile. A corresponding inward grid-construction radius is defined by

$$r_* = 2r_e - r_b. \tag{15}$$

Thus, r_e and r_* are used only to determine the spatial extent of bottom-oriented grid refinement and are not interpreted as instantaneous boundaries of the back-diffusion region.

A characteristic scale is obtained from the spreading of the migrating sedimentation boundary. For constant rotor speed, neglecting diffusion, the radial trajectory of the sedimentation boundary is approximated by

$$r_c(t) = r_m \exp(at), \tag{16}$$

which gives the estimated arrival time at radius r,

$$t_a(r) = \frac{\ln(r/r_m)}{a}. \tag{17}$$

The associated characteristic diffusion length is then defined as

$$\ell_s(r) = \sqrt{D t_a(r)}. \tag{18}$$

This scale characterizes the expected spreading of the sedimentation boundary as it propagates through the column and is used to adjust the grid spacing away from the endpoint refinement regions. The base spacing is determined near the meniscus using the reference radius

$$r_a = r_m + \delta, \qquad \delta = 0.01 \text{ cm}. \tag{19}$$

The implementation sets

$$h_0 = \min\left\{\frac{r_b - r_m}{N_0}, \frac{1}{\alpha}\sqrt{\frac{D}{a}\ln\left(\frac{r_a}{r_m}\right)}\right\}. \tag{20}$$

The first term imposes an upper bound on the nominal grid spacing, whereas the second resolves the characteristic diffusive spreading of the sedimentation boundary near the meniscus with approximately α intervals per diffusion length. For the nonuniform benchmark grids, $N_0 = 75$ and $\alpha = 5$. The parameter N_0 therefore controls the spacing cap rather than prescribing the final grid size, and the resulting number of nodes N is determined by the complete nonuniform-grid construction.

Grid construction with localized bottom refinement. When $r_* \geq \frac{r_m + r_b}{2}$, the corresponding value of $\nu = s\omega^2/D$ is relatively large, indicating sedimentation-dominated transport and a greater tendency for steep concentration gradients to develop. The grid is therefore constructed using enhanced resolution near the meniscus and the cell bottom, together with an interior spacing rule based on the spreading of the migrating sedimentation boundary. A sinusoidally graded section is first introduced near the meniscus. With $K_m = \max\{\lfloor \delta/h_0 \rfloor + 1, 5\}$, the candidate positions are

$$x_j = r_a - \delta \sin\left(\frac{j\pi}{2K_m}\right), \qquad j = K_m - 1, \ldots, 1. \tag{21}$$

Starting from r_m, the candidates are considered in increasing radial order and retained while the spacing from the previously accepted node does not exceed h_0. Let $\hat{r}_a$ denote the last accepted node in the meniscus-graded section, then

$$r_{\text{next}} = r + h_0\sqrt{\frac{\ln(r/r_m)}{\ln(\hat{r}_a/r_m)}}. \tag{22}$$

Candidates are retained while their radial positions remain strictly below r_*. Since $t_a(r) \propto \ln(r/r_m)$, this rule scales the local grid spacing with the characteristic diffusion length associated with the sedimentation-boundary arrival time, using the actual endpoint $\hat{r}_a$ of the meniscus-graded section as the reference.

Let r_L denote the last node retained by the interior-spacing rule, and define $K_b = \lfloor (r_b - r_L)/h_0 \rfloor + 1$. Starting from the cell bottom, the bottom-refined section is generated inward from the candidate positions

$$y_j = r_L + (r_b - r_L)\sin\left(\frac{j\pi}{2K_b}\right), \qquad j = K_b - 1, \ldots, 0. \tag{23}$$

Candidates are retained while their distance from the fixed cell bottom satisfies $r_b - y_j \leq h_0$. The construction terminates at the first candidate for which this condition is violated. Thus, the acceptance criterion is referenced directly to the distance from r_b, rather than to the spacing between successive accepted candidates. The remaining interval between r_L and the innermost accepted bottom node is filled using a square-root-graded transition, with additional safeguards to avoid excessively short intervals. The detailed acceptance and transition rules are given in Appendix A.

Grid construction with extended bottom refinement. When $r_* < (r_m + r_b)/2$, the corresponding value of ν is smaller, indicating a stronger relative contribution from diffusion. The equilibrium crossing radius r_e lies closer to the interior of the column, and the sedimentation profile is expected to vary more gradually over the radial domain. A separate, more globally distributed grid-allocation rule is therefore used.

$$N_{\text{est}} = \left\lfloor \frac{r_b - r_m}{h_0} \right\rfloor, \qquad K_h = \left\lfloor \frac{r_e - r_m}{h_0} \right\rfloor, \qquad K_t = N_{\text{est}} - K_h. \tag{24}$$

Between r_m and r_e, the interior nodes are distributed geometrically according to

$$x_i = r_m\left(\frac{r_e}{r_m}\right)^{(i-3/2)/(K_h-1)}, \qquad i = 2, \ldots, K_h - 1. \tag{25}$$

Between r_e and r_b, the remaining interior nodes are distributed according to

$$y_i = r_e + (r_b - r_e)\left(\frac{i}{K_t}\right)^{\gamma}, \qquad i = 1, \ldots, K_t - 1, \tag{26}$$

where $\gamma = (r_m + r_e)/(2r_e)$. The endpoints r_m and r_b are included explicitly. Among the six benchmark cases, Ex3 uses this branch, whereas the remaining five use the localized-bottom-refinement branch. The complete procedure for constructing the nonuniform underlying radial grid

Table 1
Grid parameters reproduced from the inspected implementation with $N_0 = 75$ and $\alpha = 5$. Lengths are in cm.

Case	Branch	h_0	r_*	N
Ex1	Localized	5.5813790×10^{-4}	7.1903533	167
Ex2	Localized	4.5365434×10^{-4}	7.1933432	305
Ex3	Extended	1.5027033×10^{-2}	6.1753438	93
Ex4	Localized	4.7520533×10^{-3}	6.8941685	99
Ex5	Localized	1.4535152×10^{-3}	7.1514843	110
Ex6	Localized	4.7517006×10^{-4}	7.1927810	275

is summarized in Algorithm 1, which combines the two grid-allocation branches described above. Table 1 summarizes the corresponding numerical grid parameters.

Algorithm 1 Construction of the physically informed nonuniform underlying radial grid

Require: r_m, r_b, s, D, ω; $N_0 = 75$, $\alpha = 5$, $\delta = 0.01$ cm;
Compute ν, A, r_e, $r_* = 2r_e - r_b$, and h_0 by Eq. (12), (14), (15) and (20);
if $r_* \geq (r_m + r_b)/2$ **then**
    Generate sinusoidally graded meniscus candidates;
    Retain candidates in increasing radial order while the spacing from the previous accepted node does not exceed h_0;
    Record the last accepted meniscus node as $\hat{r}_a$;
    Initialize the next interior node at $\hat{r}_a + h_0$;
    Generate subsequent interior nodes using the logarithmic spacing recurrence;
    Retain interior nodes while their radii remain strictly below r_*;
    Generate sinusoidally graded bottom candidates inward from r_b;
    Retain bottom candidates while $r_b - y_j \leq h_0$;
    Insert the square-root-graded transition using the Appendix safeguards;
    Concatenate all retained node sets in increasing radial order;
else
    Compute $N_{\mathrm{est}}, K_h, K_t$ by Eq. (24);
    Append r_m, the geometrically distributed interior nodes, and r_e;
    Append the power-law-distributed interior nodes and r_b;
end if
Store the resulting radial grid for use throughout the simulation

2.3. Prediction-assisted boundary tracking

The active node set consists of two ordered index blocks,

$$\mathcal{I}^n = \{p_n, \dots, q_n\} \cup \{u_n, \dots, N\}, \qquad q_n < u_n. \tag{27}$$

The first block resolves the migrating sedimentation boundary, whereas the second resolves the bottom region. The corresponding radial locations are denoted by

$$r_s = r_{p_n}, \quad r_p = r_{q_n}, \quad r_d = r_{u_n}. \tag{28}$$

The full concentration array is retained on the underlying radial grid, although nodes outside the active blocks do not contribute independent unknowns during the reduced solve. The radial domain is partitioned as

$$[r_m, r_s), \quad [r_s, r_p], \quad (r_p, r_d), \quad [r_d, r_b] \tag{29}$$

corresponding to the solvent plateau, sedimentation boundary region, solution plateau, and bottom region, respectively (Fig. 1(c)). The two plateau regions are masked from the reduced system, while the retained sedimentation and bottom regions remain coupled through the bridge element described below.

To prevent excessively small active blocks, a minimum block size is imposed, $m_{\min} = \lfloor 2\alpha \rfloor = 10$. For the benchmark calculations, the initial indices are set to $p_0 = 1$, $q_0 = m_{\min} + 1$, $u_0 = N - m_{\min}$, with node N retained as the physical bottom endpoint. Both the initial concentration and the solution-plateau concentration are initialized to unity. The active boundaries are updated before each time step, including the first.

Prediction windows. At time t_n, the search uses the next-step estimate

$$r_c^{n+1} = r_m \exp[a(t_n + \Delta t)]. \tag{30}$$

The characteristic diffusive spreading and the asymmetric padding lengths are defined by

$$\eta_n = \sqrt{D(t_n + \Delta t)}, \tag{31}$$

$$d_n = r_c^{n+1} \left\{ \exp[a(t_n + \Delta t)] - \exp[a(t_n - \Delta t)] \right\}, \tag{32}$$

$$L_n = 6\eta_n, \qquad R_n = 6\eta_n + d_n. \tag{33}$$

The quantity d_n is an implementation-specific additional padding term and is not interpreted as an exact characteristic displacement. The predicted sedimentation-boundary interval is therefore $[r_c^{n+1} - L_n, r_c^{n+1} + R_n]$, clipped to the physical domain $[r_m, r_b]$.

Index updates. The sedimentation-block endpoints use both the prediction windows and the stored forward differences

$$g_i^n = \frac{|c_{i+1}^n - c_i^n|}{r_{i+1} - r_i}, \qquad \varepsilon_g = 10^{-8}\ \mathrm{cm}^{-1}, \tag{34}$$

where the concentration is normalized by the initial loading. Starting from the previous sedimentation block, the inner index p_n is advanced toward larger radii and selected as the last admissible node lying to the left of the predicted interval for which $g_i^n < \varepsilon_g$. The outer index q_n is advanced from its previous position toward the bottom block until a node is found that lies beyond the predicted right boundary

and satisfies the same small-gradient criterion. The search terminates if the available separation from the previous bottom block is exhausted.

The bottom-block start u_n is updated independently of the concentration-gradient criterion. Beginning from its previous position, the search proceeds inward toward, but not including, the previous outer sedimentation index. The first admissible node satisfying $r_i < r_b - R_n$ is selected. If no such node is encountered, the previous bottom-block start is retained before subsequent consistency corrections are applied.

After these searches, the minimum-block-size constraint is enforced. The two active blocks are also required to remain ordered and non-overlapping. If necessary, the bottom-block start is reset to the node immediately following the updated sedimentation-block end.

2.4. Reduced solve and full-grid reconstruction

At each step, concentrations associated with the active indices are gathered from the stored full-grid array. The sedimentation and bottom blocks are then combined into a single ordered reduced grid. A bridge element connects the nodes r_{q_n} and r_{u_n} across the masked solution plateau, thereby coupling the two retained regions within a single tridiagonal finite element system rather than solving them independently.

Matrix entries associated with unchanged neighboring nodes are obtained from the preassembled full-grid matrices. Entries involving the two nodes adjacent to the bridge are recomputed using the bridge element spanning r_{q_n} to r_{u_n} (Fig. 1(d)), where the corresponding basis functions ϕ_{q_n} and ϕ_{u_n} are updated. When nodes on the solvent side of the sedimentation boundary are removed from the active system, their stored concentrations are set to zero. The diagonal contribution associated with the element immediately to the left of the first retained node is nevertheless preserved from the original discretization. Consequently, removal of the solvent-side nodes does not impose a new reflecting boundary condition at r_s. The resulting reduced matrices are advanced using the same Crank–Nicolson discretization as in Eq. (10).

After the reduced solve, active concentrations are scattered back to the full-grid array. Masked solvent-side nodes are set to zero. The solution-plateau value is updated by

$$c_p^{n+1} = c_p^n \exp(-2a\Delta t), \qquad c_p^0 = 1, \tag{35}$$

and all masked nodes strictly between the sedimentation and bottom blocks are assigned c_p^{n+1}. This update corresponds to the radial-dilution solution of Eq. (1) for a spatially uniform concentration field. Concentrations within the active bottom block retain the values obtained from the reduced finite element solve.

When previously masked solution-plateau nodes are reactivated, their initial values for the next reduced solve are taken from the analytically updated plateau values stored at the preceding time step. Nodes that remain active retain their numerically computed concentrations.

The analytical reconstruction of the solution plateau and the assignment of zero concentration to masked solvent-side nodes are approximation steps distinct from the Galerkin–Crank–Nicolson update. Their effects on full-column mass conservation and concentration positivity are therefore assessed separately in the numerical benchmarks. In addition, because the reduced solve contains a bridge element whereas the reconstructed full-grid profile contains a constant masked plateau, the finite element function used during the reduced solve is not identical to the subsequently stored full-grid representation.

2.5. Benchmark configurations and error evaluation

The physical parameters are listed in Table 2. The numerical reference solutions are computed on uniform grids containing 10,000 nodes. The corresponding nonuniform underlying grids contain 167, 305, 93, 99, 110, and 275 nodes for Ex1–Ex6, respectively. The reference time steps are 0.25, 0.25, 10, 5, 0.5, and 0.25 s for Ex1–Ex6, whereas the corresponding time steps used for the DBTFEM calculations are 15, 16, 2857, 536, 83, and 9 s. The physical parameter sets for Ex1 and Ex2 are identical to those used in Examples 1 and 2 of Cao and Demeler [12]. However, the output schedules, grid construction, time-step selection, and error-aggregation procedures used in the present study are defined independently. Accordingly, the calculations should be interpreted as numerical benchmarks of the present method rather than as a direct reproduction of the published ASTFEM performance comparisons.

Comparison configurations. Four numerical configurations are used to separate the effects of grid construction from those of active-node reduction: (i) active-node integration on a 10,000-node uniform grid; (ii) full-grid integration on the generated nonuniform grid; (iii) active-node integration on the nonuniform grid; and (iv) full-grid integration on a uniform grid containing the same number of nodes as the nonuniform grid. The isolated comparisons are performed for Ex1 and Ex3. Both Ex1 and Ex3 use the output schedules listed in Table 2. For these comparisons, both the full-grid and active-node solvers use $\Delta t = 0.25$ s for Ex1 and $\Delta t = 10$ s for Ex3.

Time-step selection and output times. When no positive time step is prescribed, a default step size is estimated from

$$\tau = \frac{\ln(r_b/r_m)}{s\omega^2(N-1)}. \tag{36}$$

Defining the dimensionless quantity $\tau_s = \tau/(1\ \mathrm{s})$, the implementation selects

$$\Delta t = \max\left\{2^{\lfloor \log_2 \tau_s \rfloor}, \lfloor \tau_s \rfloor\right\} \mathrm{s}. \tag{37}$$

For the benchmark cases, $\tau_s > 1$, so this rule reduces to taking the integer part of τ_s in seconds. Any positive user-specified time step overrides the default selection. For the

Table 2
Physical parameters and output times for the six DBTFEM benchmark cases. The initial concentration is normalized to unity. The final column gives the requested output times.

Case	s (S)	D (10^{-7} cm^2 s^{-1})	n_{rpm} (rpm)	r_m (cm)	r_b (cm)	Output times (s)
Ex1	10	2	60,000	6.5	7.2	750, 1125, 1500, 1875, 2250
Ex2	15.62	1.279	50,000	5.8	7.2	800, 1600, 2400, 3200, 4000
Ex3	0.3	26.953	50,000	5.8	7.2	28570, 57140, 85710, 114280, 142850
Ex4	1.5	13.477	50,000	5.8	7.2	10720, 16080, 21440, 26800, 32160
Ex5	6	5.391	50,000	6.2	7.2	2490, 3735, 4980, 6225, 7470
Ex6	30	2.695	50,000	5.8	7.2	450, 900, 1350, 1800, 2250

1 S = 10^{-13} s. The listed radii and output times define the simulation configurations used in the benchmark calculations.

numerical reference calculations, the time step is additionally constrained by the value of τ evaluated on the 10,000-node reference grid. All reference time steps listed above satisfy this constraint.

Each solver advances using complete time steps until the integration time reaches or exceeds the next requested output time. For the benchmark comparisons reported in Table 2, the requested output times are integer multiples of both the DBTFEM and reference time steps, so the corresponding profiles are evaluated at identical physical times. In separate time-step studies, however, the actual returned times are also recorded, because the integration driver neither shortens the final step to match a requested output time nor performs temporal interpolation.

Error statistics. At each requested output time t_k, the numerical and reference solutions are evaluated on a common radial sampling grid. Each solution is represented by the same piecewise linear finite element basis used in its discretization and is therefore evaluated by direct linear finite element interpolation on its own mesh. Denote the resulting sampled profiles by $S_h(\rho_j, t_k)$ and $S_{\mathrm{ref}}(\rho_j, t_k)$. The comparison grid is uniformly spaced over the closed interval $[r_m, r_b]$ with $\Delta r = 0.001$ cm. Its sampling locations are denoted by ρ_j, $j = 0, \dots, J-1$, with both physical endpoints included. The number of samples is determined by the radial interval and the prescribed sampling spacing. For example, Ex1 contains 701 sampling points, with the final point coinciding with r_b to machine precision. This common radial grid is used solely for evaluating and reporting profile deviations. It does not form part of the finite element discretization and is not used as a quadrature grid by either solver.

Define the retained sample indices and the corresponding radial interval by

$$\begin{aligned} j_- &= \lfloor 0.05J \rfloor, \qquad j_+ = \lceil 0.95J \rceil - 1, \\ \mathcal{K} &= \{j_-, \dots, j_+\}, \qquad I_{\mathrm{fit}} = [\rho_{j_-}, \rho_{j_+}], \end{aligned} \tag{38}$$

where $\mathcal{K}$ denotes the retained set of sample indices, and I_{fit} denotes the corresponding radial interval. These definitions specify the interior region used for deviation statistics, comprising approximately the central 90% of the radial sampling points. The index rule above specifies the exact subset. For K output profiles, let

$$e_{kj} = S_h(\rho_j, t_k) - S_{\mathrm{ref}}(\rho_j, t_k). \tag{39}$$

The interior maximum absolute deviation is

$$E_{\max} = \max_{\substack{1 \le k \le K \\ j \in \mathcal{K}}} |e_{kj}|, \tag{40}$$

and the pooled root-mean-square (RMS) deviation is

$$E_{\mathrm{RMS}} = \left[\frac{1}{K|\mathcal{K}|} \sum_{k=1}^{K} \sum_{j \in \mathcal{K}} e_{kj}^2 \right]^{1/2}. \tag{41}$$

The RMS deviation E_{RMS} statistic assigns equal weight to all retained radial samples and output profiles. It is not a continuous spatial L^2 norm and should not be interpreted as the maximum of the RMS deviations of the individual output profiles. No radial or volume weighting is applied. All concentration differences are normalized by the initial loading rather than by the local reference concentration.

We additionally report the maximum over the complete sampling array,

$$E_{\max}^{\mathrm{sample}} = \max_{\substack{1 \le k \le K \\ 0 \le j < J}} |e_{kj}|. \tag{42}$$

This statistic includes the sampled endpoint regions but does not represent the continuous-domain maximum over $[r_m, r_b]$. Because both profiles are evaluated using their respective piecewise linear finite element representations, the comparison introduces no additional interpolation model beyond that already inherent in the two numerical discretizations. The reference solutions are computed using the same piecewise linear finite element formulation and Crank–Nicolson time integration on a 10,000-node uniform grid with the specified reference time steps. This corresponds to the classical fixed-grid discretization of Claverie, Dreux, and Cohen [16] at high spatial resolution. The reference solutions are numerical benchmarks rather than exact solutions. Accordingly, the reported quantities measure deviations relative to these numerical references rather than absolute discretization errors.

Diagnostics at the reported output times. Additional diagnostics are evaluated from the reconstructed piecewise-linear profile directly on the complete underlying grid. Its

sector-weighted mass is evaluated exactly as

$$M_h(t_k) = \sum_{i=1}^{N-1} \frac{r_{i+1} - r_i}{6} \big[(2r_i + r_{i+1})c_i(t_k) + (r_i + 2r_{i+1})c_{i+1}(t_k)\big]. \tag{43}$$

Both active and reconstructed masked nodes contribute to this integral. The maximum relative mass deviation and the minimum nodal concentration over the reported output times are defined as

$$E_M^{\text{out}} = \max_{1\le k\le K} \left| \frac{M_h(t_k)}{M(0)} - 1 \right|, \tag{44}$$

$$C_{\min}^{\text{out}} = \min_{\substack{1\le k\le K \\ 1\le i\le N}} c_i(t_k). \tag{45}$$

The active fraction at output time t_k is

$$f_{\text{act}}(t_k) = \frac{(q_k - p_k + 1) + (N - u_k + 1)}{N}. \tag{46}$$

This quantity measures the instantaneous fraction of spatial degrees of freedom retained by the active-node formulation at the sampled output time. These diagnostics characterize only the reported output states. In particular, E_M^{out} does not bound mass deviations that may occur at intermediate time steps or during active-set reconfiguration, and values of f_{act} sampled at the output times should not be interpreted as time-averaged activity.

Use of AI-assisted tools in code preparation. The AI tool `WorkBuddy`, using the DeepSeek-V4.1-Flash model, was used only to assist in refactoring and documenting the auxiliary test and post-processing scripts that generate the tables and figures from solver output. It was not used in the design or implementation of the numerical algorithm or of the solver. The algorithm design and solver code were developed entirely by the authors. All AI-assisted changes to the auxiliary scripts were reviewed, tested, and verified by the authors before use.

3. Results

3.1. Effect of nonuniform radial grid allocation

The grid generated for Ex1 contains 167 nodes and allocates fine resolution near the meniscus and the cell bottom (Fig. 2). To isolate grid allocation, full-grid finite element solutions were computed on nonuniform and uniform grids with the same number of nodes and the same time step. Active-node masking was disabled in these comparisons.

For Ex1, with $N = 167$ and $\Delta t = 0.25$ s, the nonuniform grid gives $E_{\max} = 1.72062 \times 10^{-3}$ and $E_{\text{RMS}} = 2.94611 \times 10^{-4}$. The corresponding uniform-grid values are 1.73660 and 8.19566×10^{-2}, respectively (Fig. 3). Thus, at this node count and time step, nonuniform allocation substantially reduces the interior-profile deviations in the steep-boundary case.

For Ex3, with $N = 93$ and $\Delta t = 10$ s, the nonuniform grid gives $E_{\max} = 2.45500 \times 10^{-4}$ and $E_{\text{RMS}} = 5.75346 \times 10^{-5}$. The uniform-grid values are 2.84736×10^{-4} and 6.12452×10^{-5}. Both comparisons indicate similar error scales for the two Ex3 grids. The examples illustrate a case-dependent benefit rather than an optimality result or a general convergence rate.

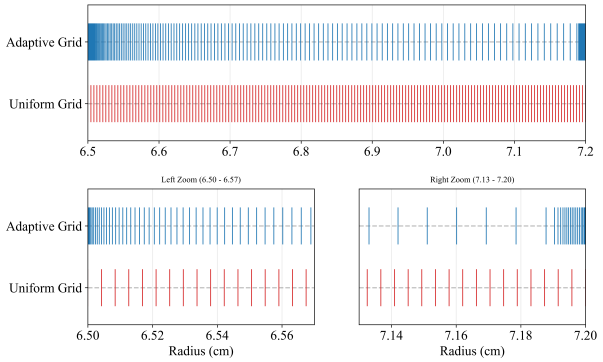

Figure 2: Fixed nonuniform radial grid generated for Ex1 with $N_0 = 75$ and $\alpha = 5$, giving $N = 167$ nodes. The coordinates are determined before time integration. Subsequent boundary tracking changes the active node set rather than these coordinates.

3.2. Effect of active-node masking

Fig. 4 illustrates the selection of active sedimentation and bottom regions in Ex1. The intermediate solution plateau is represented by analytical dilution values after each reduced solve. As the active blocks expand, previously masked nodes can re-enter the numerical calculation. The bottom block retains the concentration values returned by the solver.

To isolate masking, active-grid and full-grid calculations were compared on the same 10,000-node uniform grid and at the same time step (Fig. 5). For Ex1, $\Delta t = 0.25$ s gives $E_{\max} = 1.59175 \times 10^{-5}$ and $E_{\text{RMS}} = 3.67802 \times 10^{-6}$. For Ex3, $\Delta t = 10$ s gives $E_{\max} = 6.48327 \times 10^{-7}$ and $E_{\text{RMS}} = 1.83666 \times 10^{-7}$. These differences quantify the effect of masking and reconstruction for the specified fine-grid calculations and output schedules. They do not directly measure the masking contribution on the coarser nonuniform grids, full-column mass drift, or discrepancies at the physical endpoints.

3.3. Combined method across six cases

Table 3 reports the combined use of the nonuniform grid and active-node integration. Underlying node counts range from 93 to 305, with time steps selected as described in Methods. Fig. 6 shows representative profiles for Ex1 and Ex3. Across all six cases, $E_{\max}$ ranges from 6.39354×10^{-4} to 3.42704×10^{-2}, and E_{RMS} ranges from 1.01629×10^{-4} to 3.50517×10^{-3}. These are absolute deviations in loading-normalized concentration, evaluated on the central sample interval at the output times in Table 2.

The combined errors include spatial discretization, time stepping, and active-node reconstruction. Accordingly, the differences between these results and the isolated fine-grid

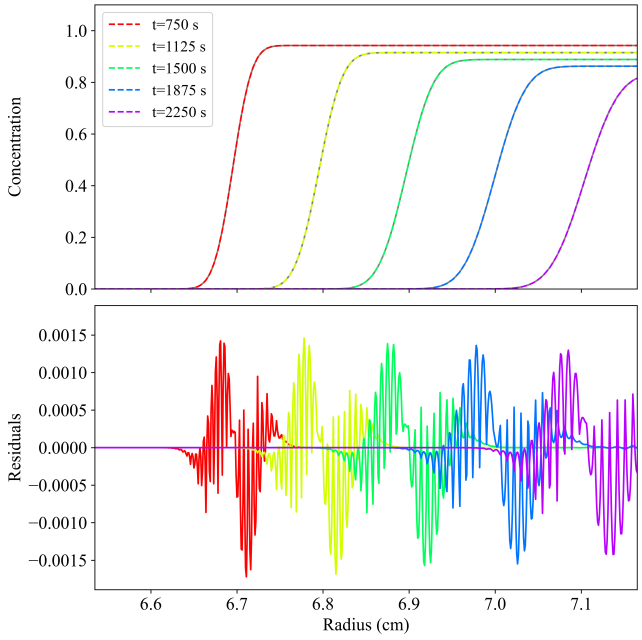

(a) Ex1: nonuniform grid.

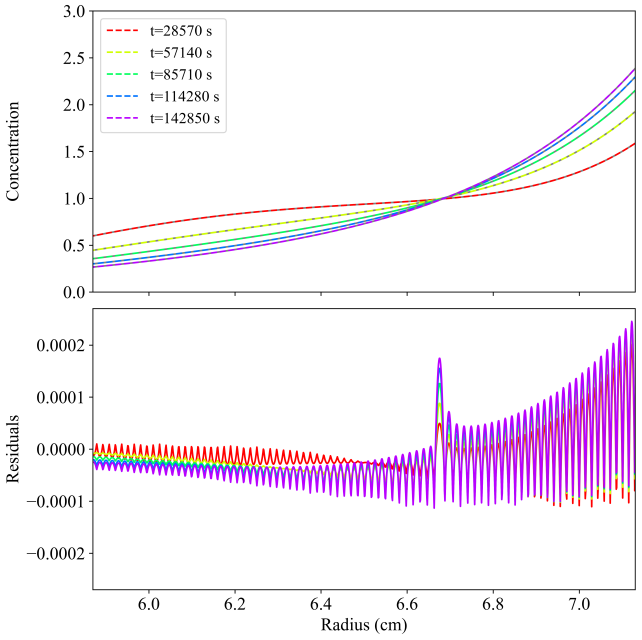

(b) Ex3: nonuniform grid.

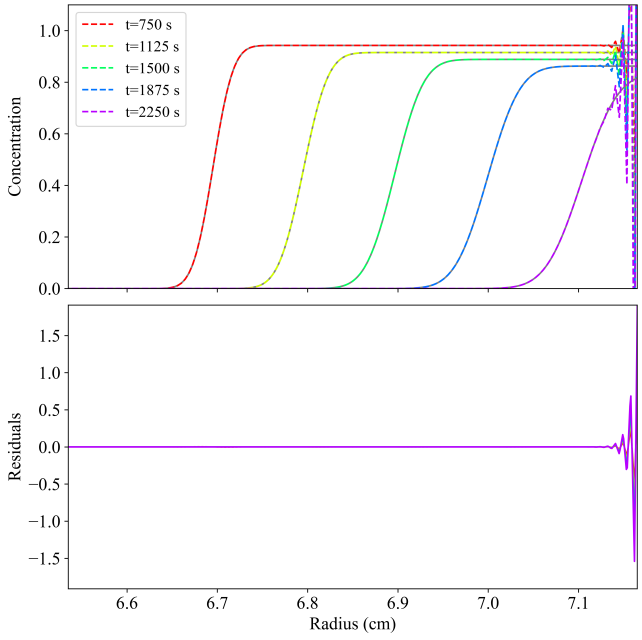

(c) Ex1: uniform grid.

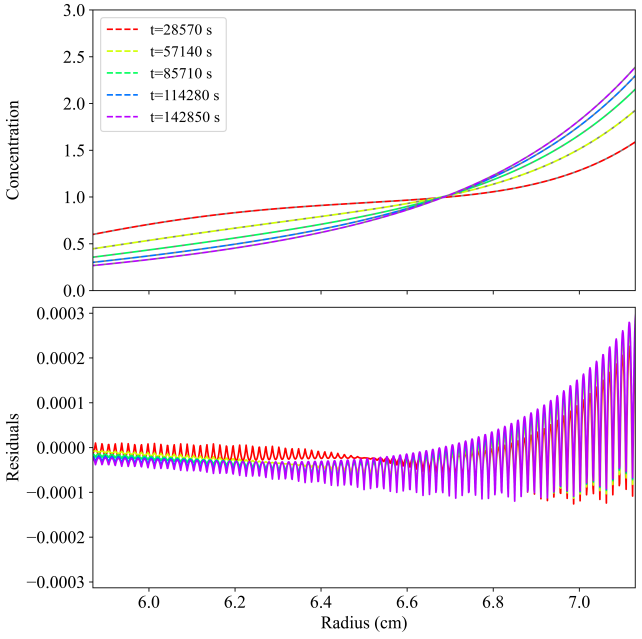

(d) Ex3: uniform grid.

Figure 3: Effect of grid allocation with masking disabled. Ex1 uses $N = 167$ and $\Delta t = 0.25$ s; Ex3 uses $N = 93$ and $\Delta t = 10$ s. Gray curves show the corresponding 10,000-node uniform-grid references at the same time steps. Ex1 output times are 750, 1125, 1500, 1875, and 2250 s. Ex3 output times are 28570, 57140, 85710, 114280, and 142850 s. Panels show the central approximately 90% of radial samples. Error statistics are pooled over these samples and all displayed output times as defined in Eqs. (40) and (41).

masking results cannot be assigned to masking alone. The interior statistics also exclude the outermost portions of the column and do not establish accuracy throughout the bottom accumulation region. The complete-array maxima in Table 3 range from 0.0156758 to 15.7644. Their much larger values show that the interior error does not represent the entire sampled column. A large loading-normalized difference alone does not identify its cause: bottom accumulation can produce concentrations far above the initial loading, and spatial resolution and time stepping can both contribute. We therefore do not attribute the complete-array deviations solely to numerical oscillations.

Table 3
Combined-method deviations from the specified numerical references. N is the fixed underlying node count and all reference grids have 10,000 nodes. Interior maximum and pooled RMS are defined by Eqs. (40) and (41); $E_{\max}^{\text{sample}}$ uses the complete comparison array as defined in Eq. (42). The combined-method output schedules are given in Table 2.

Case	N	Δt (s)	Δt_{ref} (s)	$E_{\max}$	E_{RMS}	$E_{\max}^{\text{sample}}$
Ex1	167	15	0.25	1.80092×10^{-2}	2.99123×10^{-3}	2.10565
Ex2	305	16	0.25	3.42704×10^{-2}	3.44277×10^{-3}	5.21139
Ex3	93	2857	10	6.39354×10^{-4}	1.01629×10^{-4}	0.0156758
Ex4	99	536	5	4.83859×10^{-3}	4.70320×10^{-4}	0.0375675
Ex5	110	83	0.5	4.91671×10^{-3}	1.06034×10^{-3}	0.896950
Ex6	275	9	0.25	3.35569×10^{-2}	3.50517×10^{-3}	15.7644

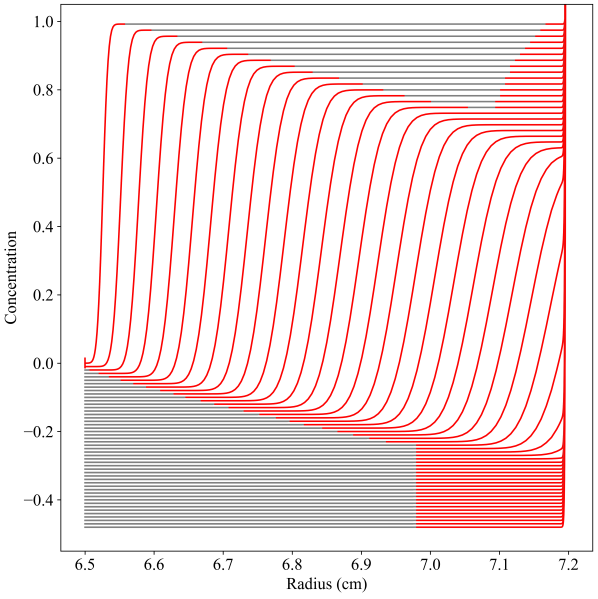

Figure 4: Illustration of active-node selection in Ex1. Red portions indicate retained boundary regions and gray portions indicate masked regions. Profiles after the first are shifted downward for display. This plot illustrates the selection process; it is not a runtime benchmark or a quantitative record of the active-node fraction.

3.4. Time-step sensitivity

For Ex1 on the 167-node nonuniform grid, reducing Δt from 18.75 s to 1 s lowers $E_{\max}$ from approximately 2.79×10^{-2} to 1.70×10^{-3} (Table 4). Further reduction to 0.5 and 0.25 s changes $E_{\max}$ only slightly, and in the direction opposite to the temporal trend: the interior maximum drifts upward over this final range, whereas the pooled RMS continues to decrease slightly. This behavior is consistent with a residual error level set by spatial discretization and other non-temporal contributions. A fixed-grid time-step study alone does not establish the convergence order or identify a unique source of the residual error.

3.5. Diagnostics at the reported output times

Table 5 summarizes checks on the reconstructed piecewise-linear profiles. The output-sampled maximum relative mass changes are below 4.11×10^{-6} for all six cases, but this observation does not prove exact conservation or bound the changes at unrecorded time steps. Negative nodal concentrations occur in several cases, including a minimum of approximately -0.0498 in Ex5. Thus, small mass drift is compatible with a failure of non-negativity.

Table 4
Time-step sensitivity for combined-method Ex1 with $N = 167$. The reference has $N_{\text{ref}} = 10{,}000$ and $\Delta t_{\text{ref}} = 0.25$ s. The same Ex1 output times and central sample interval are used for every row.

Δt (s)	$E_{\max}$	E_{RMS}
0.25	1.72062×10^{-3}	2.94611×10^{-4}
0.5	1.71568×10^{-3}	2.94709×10^{-4}
1	1.69538×10^{-3}	2.95305×10^{-4}
5	2.51866×10^{-3}	4.48622×10^{-4}
7.5	4.73559×10^{-3}	8.05975×10^{-4}
15	1.80092×10^{-2}	2.99123×10^{-3}
18.75	2.79338×10^{-2}	4.65280×10^{-3}

The active fractions are also configuration dependent. Ex1 retains approximately 33.5%–46.7% of its underlying nodes at the reported outputs, whereas all underlying nodes are active for Ex3 and Ex4 at their reported outputs. These ranges neither describe activity throughout the entire trajectory nor establish a runtime reduction.

4. Discussion

The comparisons separate two contributions to the DBT-FEM. Nonuniform grid allocation improves the use of a fixed number of degrees of freedom, particularly for the steep-boundary Ex1 case. Active-node selection additionally reduces the dimension of the linear system when sufficiently broad solvent or solution plateaus are present. The similar uniform and nonuniform errors for Ex3 show that the benefit of grid allocation depends on the transport regime and the requested accuracy.

The method retains a finite-column bottom region and couples it to the sedimentation region through a bridge element. Masked solution nodes are subsequently filled using the analytical dilution relation. This sequence is important: the computed bottom concentrations are retained, while the bridge representation and the reconstructed full-grid profile

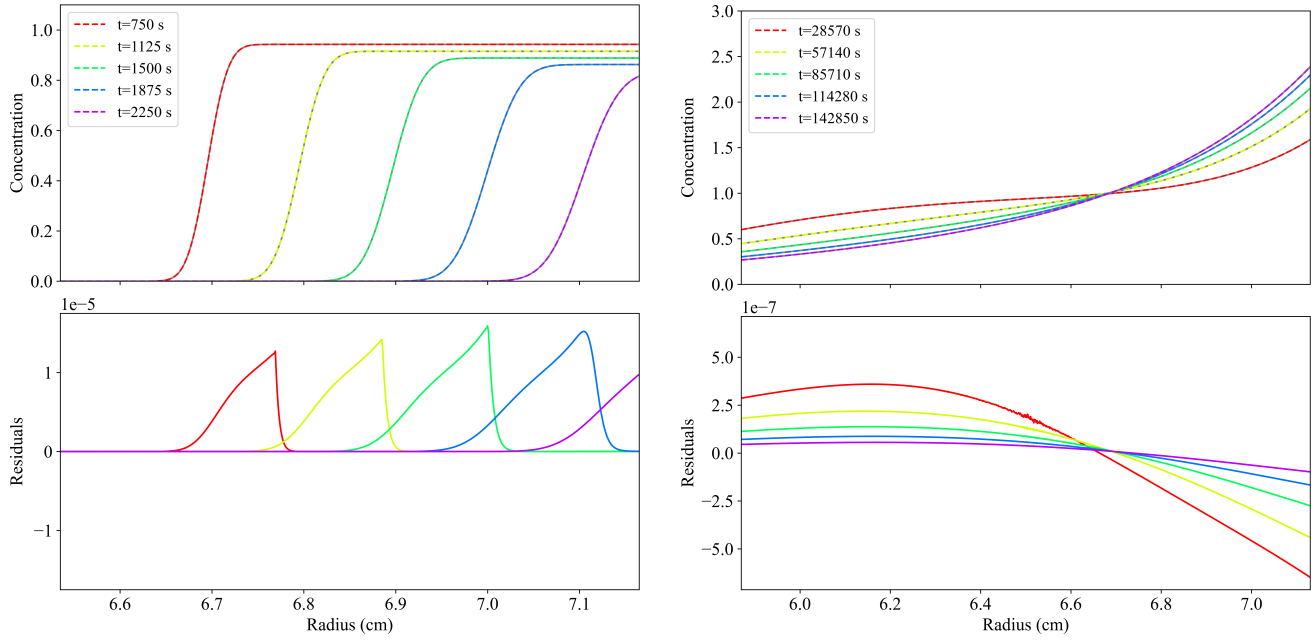

(a) Ex1: $\Delta t = 0.25$ s.

(b) Ex3: $\Delta t = 10$ s.

Figure 5: Isolated masking comparison on 10,000-node uniform grids. The active-grid solutions are compared with full-grid references (gray) at identical time steps. Physical parameters are given in Table 2; output times are 750, 1125, 1500, 1875, and 2250 s for Ex1 and 28570, 57140, 85710, 114280, and 142850 s for Ex3. Only the central approximately 90% of radial samples are displayed and used in the reported interior error statistics.

Table 5
Diagnostics evaluated at the reported DBTFEM output times. E_M^{out} is the maximum relative mass deviation, $C_{\min}^{\text{out}}$ is the minimum nodal concentration, and the reported f_{act} interval gives the range of active-node fractions over the sampled output times.

Case	E_M^{out}	$C_{\min}^{\text{out}}$	Range of f_{act}
Ex1	4.10493×10^{-6}	-3.61905×10^{-9}	0.3353–0.4671
Ex2	3.91171×10^{-6}	-3.33101×10^{-3}	0.3082–0.4000
Ex3	8.49109×10^{-7}	0.237932	1.0000–1.0000
Ex4	1.52305×10^{-6}	-2.85183×10^{-3}	1.0000–1.0000
Ex5	1.60062×10^{-6}	-4.97874×10^{-2}	0.7182–1.0000
Ex6	3.98256×10^{-6}	-2.68772×10^{-3}	0.2655–0.3927

are distinct approximations. The small differences in the fine-grid masking experiments support this approximation for the tested interior profiles. They do not prove that reconstruction is conservative or that bottom concentrations are equally accurate.

The grid construction is physically informed but includes several prescribed design choices, such as the base-spacing factor, the equilibrium-based refinement scale, and the selection between two grid-construction branches. Prediction-assisted boundary tracking likewise employs prescribed padding parameters and a concentration-gradient threshold for identifying the sedimentation block. The present formulation should therefore be regarded as a practical grid-allocation and active-node-selection strategy rather than as an analytically optimal mesh or an a posteriori error-controlled adaptive method. The underlying radial coordinates remain fixed throughout each simulation.

The numerical evidence has several limits. First, the complete-array deviations are much larger than the interior statistics. Resolving a finite-domain boundary condition does not by itself establish accurate bottom profiles, and sampling the stored nodal solutions on a discrete array is not an evaluation of the continuous finite element solutions. Second, the reconstructed profiles exhibit small output-sampled mass drift but can have negative nodal values. Monitoring all time steps and the states immediately before and after reconstruction is needed to separate these effects. Interior concentration errors cannot be compared interchangeably with a relative mass-conservation tolerance or with an experimental noise standard deviation from a different measurement setting. Third, the fine-grid references share the underlying discretization; reference refinement or an independent solver is needed to assess their remaining error.

The active-node count is also time- and case-dependent. When the two active regions cover the column, plateau

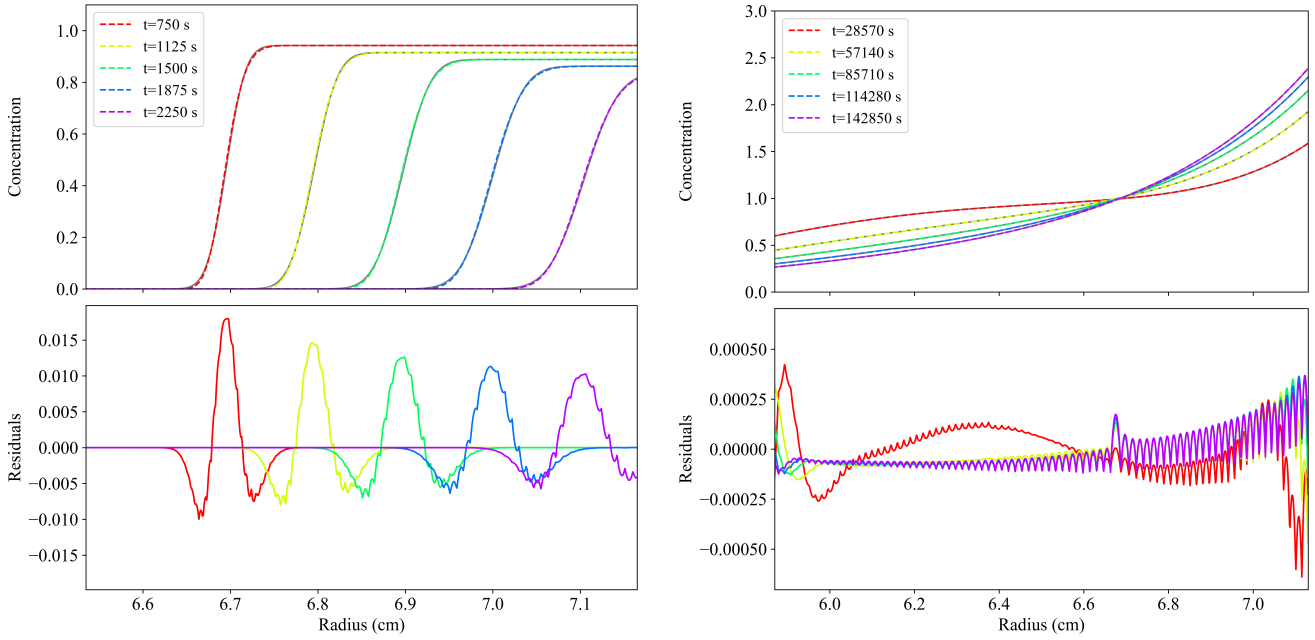

(a) Ex1: $N = 167$, $\Delta t = 15$ s.

(b) Ex3: $N = 93$, $\Delta t = 2857$ s.

Figure 6: Representative combined-method profiles. Gray curves are 10,000-node uniform-grid reference solutions, using time steps of 0.25 s for Ex1 and 10 s for Ex3. Output times are specified in Table 2. For Ex1, $(E_{\max}, E_{\mathrm{RMS}}) = (1.80092\times10^{-2}, 2.99123\times10^{-3})$; for Ex3, the corresponding values are $(6.39354\times10^{-4}, 1.01629\times10^{-4})$. Displayed profiles and reported statistics concern the central approximately 90% of radial samples.

masking offers little or no reduction of the linear-system dimension. Moreover, fewer active unknowns do not translate directly into a measured speedup: index updates, matrix extraction, reconstruction, and repeated factorization contribute to runtime. The present comparisons establish error levels, underlying grid sizes, and output-sampled activity, but do not provide an isolated runtime benchmark. A performance comparison should measure the solvers under matched accuracy requirements, output times, hardware, and implementation conditions.

For the same reason, published ASTFEM configurations [12] provide useful context but cannot establish a relative accuracy–runtime advantage without a matched comparison. Node counts and time steps alone are insufficient to infer computational cost across methods. We therefore make no quantitative speedup claim relative to ASTFEM or other established Lamm-equation solvers.

Finally, the use of linear finite elements and Crank–Nicolson integration does not by itself establish a convergence order for the complete algorithm. Changing active sets, bridging, and analytical plateau replacement introduce additional approximation steps. Separate spatial and temporal refinement studies, with masking both enabled and disabled, are required to quantify their effects. The current tests are restricted to ideal single solutes at constant rotor speed. Extensions to variable-speed runs, concentration-dependent transport, or interacting systems require additional formulation and validation.

5. Conclusions

The DBTFEM provides a finite element formulation for the finite-column Lamm equation that combines a fixed, physically informed nonuniform radial grid with dynamic selection of nodes associated with the migrating sedimentation boundary and the bottom region. The retained regions are coupled through a bridge element, while concentrations in the masked solution plateau are reconstructed analytically using the radial-dilution solution. Across six benchmark cases using underlying grids of 93–305 nodes, the maximum interior deviations from the specified high-resolution numerical references range from 6.39×10^{-4} to 3.43×10^{-2}. Separate comparisons of grid allocation and active-node masking show that the benefit of nonuniform grid placement is strongly profile dependent. A substantial improvement is obtained for the steep-boundary Ex1 case, whereas the broader-profile Ex3 case shows similar interior accuracy on uniform and nonuniform grids. The active-node formulation can further reduce the number of spatial degrees of freedom when the sedimentation and bottom regions remain sufficiently separated.

The largest discrepancies occur near the radial endpoints, where complete-array deviations can be substantially greater than those measured over the interior region. The output diagnostics also show that small relative mass deviations alone do not guarantee non-negative concentrations. These observations identify endpoint treatment, reconstruction accuracy, and independent convergence of the numerical reference solutions as important areas for further validation.

Direct runtime benchmarking is also required to quantify the computational benefit associated with the reduced active-node systems.

Overall, the present results show that DBTFEM can reproduce interior sedimentation profiles with substantially reduced spatial resolution for a range of transport regimes, while providing a framework for concentrating computational effort on the dynamically relevant regions of the solution domain.

A. Detailed construction of the nonuniform radial grid

This supplement specifies the list operations used to generate the positive-sedimentation grids in the benchmark calculations. The notation follows Methods: $a = s\omega^2$, $\nu = a/D$, $r_a = r_m + 0.01$ cm, $h_0 = \min\{(r_b - r_m)/N_0, \ell_s(r_a)/\alpha\}$, and $r_* = 2r_e - r_b$. All floor operations refer to the mathematical floor for positive arguments.

A.1. Localized bottom region

This branch is used when $r_* \geq (r_m + r_b)/2$.

Meniscus list. Initialize the ordered list $\mathcal{R} = [r_m]$ and set $K_m = \max\{\lfloor (r_a - r_m)/h_0 \rfloor + 1, 5\}$. For $j = K_m - 1, K_m - 2, \ldots, 1$, calculate

$$x = r_a - (r_a - r_m)\sin\left(\frac{j\pi}{2K_m}\right).$$

If $x - \mathcal{R}_{\text{last}} > h_0$, stop this loop. Otherwise append x to $\mathcal{R}$. Set $\hat{r}_a = \mathcal{R}_{\text{last}}$. The loop does not explicitly append r_a.

Interior list. Set $x = \hat{r}_a + h_0$. While $x < r_*$, append x to $\mathcal{R}$ and replace it by

$$x \leftarrow x + h_0\sqrt{\frac{\ln(x/r_m)}{\ln(\hat{r}_a/r_m)}}.$$

Set $r_L = \mathcal{R}_{\text{last}}$. Thus r_L, rather than r_* itself, is the anchor of the bottom construction. The code does not force a node at r_*.

Bottom list. Set $K_b = \lfloor (r_b - r_L)/h_0 \rfloor + 1$ and initialize the ordered bottom list $\mathcal{B} = [r_b]$. For $j = K_b - 1, K_b - 2, \ldots, 0$, calculate

$$y = r_L + (r_b - r_L)\sin\left(\frac{j\pi}{2K_b}\right).$$

If $r_b - y > h_0$, stop this loop. Otherwise prepend y to $\mathcal{B}$. Let $r_B = \mathcal{B}_{\text{first}}$ after the loop. The last entry of $\mathcal{B}$ remains r_b throughout this construction. The retained sinusoidal candidates therefore lie within a distance h_0 of the cell bottom.

Transition list and assembly. Set $K_t = \lfloor (r_B - r_L)/h_0 \rfloor$. For $i = 1, \ldots, K_t - 1$, compute the candidate

$$z = r_L + (r_B - r_L)\sqrt{\frac{i}{K_t}},$$

and apply the following operations in the stated order:

1. If $z - \mathcal{R}_{\text{last}} < h_0$, set $z = \mathcal{R}_{\text{last}} + h_0$. If this replacement gives $z > r_B$, terminate the loop.
2. If $z \geq r_B - 0.25h_0$, terminate the loop.
3. Otherwise, if $z \geq r_B - 0.5h_0$, replace z by $(\mathcal{R}_{\text{last}} + r_B)/2$.
4. Append z to $\mathcal{R}$.

Finally append the entire list $\mathcal{B}$ to $\mathcal{R}$. The last point is r_b. These explicit transition rules are part of the implementation and are not replaced by a generic monotone-spacing assumption.

A.2. Extended bottom region

This branch is used when $r_* < (r_m + r_b)/2$. Set

$$N_{\text{est}} = \left\lfloor \frac{r_b - r_m}{h_0} \right\rfloor,$$
$$K_h = \left\lfloor \frac{r_e - r_m}{h_0} \right\rfloor, \qquad K_t = N_{\text{est}} - K_h.$$

Initialize $\mathcal{R} = [r_m]$. Append, in increasing index order,

$$x_i = r_m\left(\frac{r_e}{r_m}\right)^{(i-3/2)/(K_h-1)}, \qquad i = 2, \ldots, K_h - 1.$$

Append r_e, followed by

$$y_i = r_e + (r_b - r_e)\left(\frac{i}{K_t}\right)^{(r_m+r_e)/(2r_e)}, \qquad i = 1, \ldots, K_t - 1.$$

Finally append r_b. For the nondegenerate benchmark parameters, the resulting list contains $K_h + K_t = N_{\text{est}}$ nodes.

CRediT authorship contribution statement

Chengshi Zeng: Methodology, Software, Data curation, Writing – original draft, Visualization, Validation. **Xinqi Gong:** Writing – original draft, Supervision, Methodology, Formal analysis. **Wenqi Li:** Conceptualization, Writing – original draft, Writing – review & editing, Supervision, Resources, Methodology.

Declaration of competing interest

The authors declare that they have no known competing financial interests or personal relationships that could have appeared to influence the work reported in this paper.

Code availability

The finite element solver, the grid-generation routines, and the scripts that reproduce the tables and figures of this work are available at `https://www.frcbs.tsinghua.edu.cn/gitlab/zengchengshi/dbtfem`.

Declaration of generative AI and AI-assisted technologies in the writing process

During the preparation of this work the author(s) used `WorkBuddy`, using the DeepSeek-V4.1-Flash model, in order to improve the clarity and language of the text. After using this tool, the author(s) reviewed and edited the content as needed and take(s) full responsibility for the content of the publication. The AI-assisted preparation of the auxiliary test and post-processing scripts is a research-process use and is described separately in the Methods section.

References

[1] D. A. Yphantis, Equilibrium ultracentrifugation of dilute solutions, Biochemistry 3 (3) (1964) 297–317. doi:10.1021/bi00891a003.

[2] T. Svedberg, K. O. Pedersen, The Ultracentrifuge, Clarendon Press, Oxford, 1940.

[3] H. Fujita, Mathematical Theory of Sedimentation Analysis, Academic Press, New York, 1962.

[4] P. Schuck, Sedimentation Velocity Analytical Ultracentrifugation: Discrete Species and Size-Distributions of Macromolecules and Particles, CRC Press, Taylor & Francis Group, Boca Raton, FL, 2016.

[5] O. Lamm, Die differentialgleichung der ultrazentrifugierung, Arkiv för matematik, astronomi och fysik 21B (2) (1929) 1–4.

[6] P. Schuck, Sedimentation analysis of noninteracting and self-associating solutes using numerical solutions to the Lamm equation, Biophysical Journal 75 (3) (1998) 1503–1512. doi:10.1016/S0006-3495(98)74069-X.

[7] K. E. van Holde, W. O. Weischet, Boundary analysis of sedimentation-velocity experiments with monodisperse and paucidisperse solutes, Biopolymers 17 (6) (1978) 1387–1403. doi:10.1002/bip.1978.360170602.

[8] W. F. Stafford, Boundary analysis in sedimentation transport experiments: a procedure for obtaining sedimentation coefficient distributions using the time derivative of the concentration profile, Analytical Biochemistry 203 (2) (1992) 295–301. doi:10.1016/0003-2697(92)90316-Y.

[9] P. Schuck, Size-distribution analysis of macromolecules by sedimentation velocity ultracentrifugation and lamm equation modeling, Biophysical Journal 78 (3) (2000) 1606–1619. doi:10.1016/S0006-3495(00)76713-0.

[10] P. H. Brown, P. Schuck, Macromolecular size-and-shape distributions by sedimentation velocity analytical ultracentrifugation, Biophysical Journal 90 (12) (2006) 4651–4661. doi:10.1529/biophysj.106.081372.

[11] E. Brookes, W. Cao, B. Demeler, A two-dimensional spectrum analysis for sedimentation velocity experiments of mixtures with heterogeneity in molecular weight and shape, European Biophysics Journal 39 (3) (2010) 405–414. doi:10.1007/s00249-009-0413-5.

[12] W. Cao, B. Demeler, Modeling analytical ultracentrifugation experiments with an adaptive space-time finite element solution of the lamm equation, Biophysical Journal 89 (3) (2005) 1589–1602. doi:https://doi.org/10.1529/biophysj.105.061135.

[13] P. H. Brown, P. Schuck, A new adaptive grid-size algorithm for the simulation of sedimentation velocity profiles in analytical ultracentrifugation, Computer Physics Communications 178 (2) (2008) 105–120. doi:https://doi.org/10.1016/j.cpc.2007.08.012.

[14] J. Liu, C. Chen, A characteristic finite element method with local mesh refinements for the lamm equation in analytical ultracentrifugation, Numerical Methods for Partial Differential Equations 25 (2) (2009) 292–310. doi:https://doi.org/10.1002/num.20344.

[15] M. Dishon, G. H. Weiss, D. A. Yphantis, Numerical solutions of the lamm equation. i. numerical procedure, Biopolymers 4 (4) (1966) 449–455.

[16] J.-M. Claverie, H. Dreux, R. Cohen, Sedimentation of generalized systems of interacting particles. i. solution of systems of complete lamm equations, Biopolymers 14 (8) (1975) 1685–1700. doi:https://doi.org/10.1002/bip.1975.360140811.

[17] B. Demeler, H. Saber, Determination of molecular parameters by fitting sedimentation data to finite-element solutions of the lamm equation, Biophysical Journal 74 (1) (1998) 444–454. doi:10.1016/S0006-3495(98)77802-6.

[18] W. Huang, Y. Ren, R. D. Russell, Moving mesh methods based on moving mesh partial differential equations, Journal of Computational Physics 113 (2) (1994) 279–290. doi:10.1006/jcph.1994.1135.

[19] W. Cao, B. Demeler, Modeling analytical ultracentrifugation experiments with an adaptive space-time finite element solution for multicomponent reacting systems, Biophysical Journal 95 (1) (2008) 54–65. doi:10.1529/biophysj.107.123950.

[20] J. Crank, P. Nicolson, A practical method for numerical evaluation of solutions of partial differential equations of the heat-conduction type, Mathematical Proceedings of the Cambridge Philosophical Society 43 (1) (1947) 50–67. doi:10.1017/S0305004100023197.

[21] C. A. Brautigam, Using Lamm-equation modeling of sedimentation velocity data to determine the kinetic and thermodynamic properties of macromolecular interactions, Methods 54 (1) (2011) 4–15. doi:10.1016/j.ymeth.2010.12.029.

[22] P. Schuck, B. Demeler, Direct sedimentation analysis of interference optical data in analytical ultracentrifugation, Biophysical Journal 76 (1999) 2288–2296. doi:10.1016/S0006-3495(99)77384-4.

[23] S. Mortezazadeh, B. Demeler, Systematic noise removal from analytical ultracentrifugation data with UltraScan, European Biophysics Journal 52 (4-5) (2023) 203–213. doi:10.1007/s00249-023-01631-6.